Monthly Notices
of the
ROYAL ASTRONOMICAL SOCIETY

MNRAS **488,** 2412–2422 (2019)
Advance Access publication 2019 July 11

doi:10.1093/mnras/stz1933

Shocks in relativistic viscous accretion flows around Kerr black holes

Indu K. Dihingia,[1] Santabrata Das ,[1]★ Debaprasad Maity[1] and Anuj Nandi[2]

[1]*Indian Institute of Technology Guwahati, Guwahati 781039, Assam, India*
[2]*Space Astronomy Group, ISITE Campus, U. R. Rao Satellite Center, Outer Ring Road, Marathahalli, Bangalore 560037, India*

Accepted 2019 July 9. Received 2019 July 9; in original form 2019 March 15

ABSTRACT

We study the relativistic viscous accretion flows around the Kerr black holes. We present the governing equations that describe the steady-state flow motion in full general relativity and solve them in 1.5D to obtain the complete set of global transonic solutions in terms of the flow parameters, namely specific energy ($\mathcal{E}$), specific angular momentum ($\mathcal{L}$), and viscosity (α). We obtain a new type of accretion solution which was not reported earlier. Further, we show for the first time to the best of our knowledge that viscous accretion solutions may contain shock waves particularly when flow simultaneously passes through both inner critical point ($r_{\rm in}$) and outer critical point ($r_{\rm out}$) before entering into the Kerr black holes. We examine the shock properties, namely shock location ($r_{\rm s}$) and compression ratio (R, the measure of density compression across the shock front) and show that shock can form for a large region of parameter space in $\mathcal{L}$–$\mathcal{E}$ plane. We study the effect of viscous dissipation on the shock parameter space and find that parameter space shrinks as α is increased. We also calculate the critical viscosity parameter ($\alpha^{\rm cri}$) beyond which standing shock solutions disappear and examine the correlation between the black hole spin ($a_{\rm k}$) and $\alpha^{\rm cri}$. Finally, the relevance of our work is conferred where, using $r_{\rm s}$ and R, we empirically estimate the oscillation frequency of the shock front ($\nu_{\rm QPO}$) when it exhibits quasi-periodic (QP) variations. The obtained results indicate that the present formalism seems to be potentially viable to account for the QPO frequency in the range starting from milli-Hz to kilo-Hz as 0.386 Hz $\leq \nu_{\rm QPO}(\frac{10\,{\rm M}_\odot}{M_{\rm BH}}) \leq$ 1312 Hz for $a_{\rm k} = 0.99$, where $M_{\rm BH}$ stands for the black hole mass.

Key words: accretion, accretion discs – black hole physics – hydrodynamics – shock waves.

1 INTRODUCTION

The accretion process on to a black hole is believed to be the most efficient energy release mechanism because of the fact that it is an order of magnitude stronger than the nuclear fusion reactions (Frank, King & Raine 2002). As black holes themselves do not emit any radiation therefore one compels to rely on the study of accretion flows in order to understand the astrophysical black holes. And, because of the strong gravity of the black holes, it is necessary to examine the relativistic accretion flows considering the general relativistic framework.

In the early seventies, a comprehensive study of relativistic accretion flow around the Kerr black holes was carried out by Novikov & Thorne (1973). Later, Fukue (1987) examined the transonic properties of the inflowing matter considering full relativistic treatment. Riffert & Herold (1995) reported the correct description of the thin accretion disc structure around the Kerr black holes. Meanwhile, Chakrabarti (1996a,b) examined the relativistic accretion flow assuming weak viscosity limit and Peitz & Appl (1997) studied the relativistic viscous accretion flow considering the polytropic equation of state. Subsequently, Gammie & Popham (1998) and Popham & Gammie (1998) pointed out the importance of relativistic equation of state (EoS) while studying the relativistic accretion flow. Chattopadhyay & Chakrabarti (2011) investigated the effect of fluid composition on the accretion flow properties around the Schwarzschild black holes. Recently, Chattopadhyay & Kumar (2016) studied the accretion–ejection solutions in full general relativity considering non-rotating black holes, and they extended the work further for rotating black holes as well (Kumar & Chattopadhyay 2017).

It may be noted that some of the above studies examined the phenomena of shock waves where accretion flow variables encounter discontinuous transitions (Fukue 1987; Chakrabarti 1996a,b; Chattopadhyay & Chakrabarti 2011; Chattopadhyay & Kumar 2016; Kumar & Chattopadhyay 2017). In reality, there are various astrophysical phenomena associating the shock waves, namely supernova explosions, various outburst phenomena, shocks in astrophysical jets and winds (Fukue 2019). This truly indicates that shocks are common in astrophysical environments. However,

★ E-mail: sbdas@iitg.ac.in

the study of shock waves in the relativistic viscous accretion flow around the Kerr black holes remains unexplored till date. In this context, questions naturally arise whether shocks continue to be present or not under strong gravity? If so, what would be the influence of the relativistic EoS on the shock properties? How is the shock location affected due to the viscosity as well as the black hole spin? Can the modulation of shock front render the quasi-periodic oscillation (QPO) phenomena commonly observed in Galactic black hole (GBH) sources? In this work, for the first time to our knowledge, we intend to answer these questions.

In an accretion process, rotating matter begins its journey towards the black hole with negligible radial velocity from the outer edge of the disc. As the flow moves inward, the radial velocity gradually increases and eventually, subsonic flow changes its sonic state at the critical point to become supersonic before crossing the event horizon. Depending on the input parameters, the flow may contain multiple critical points, and in general, the flow of this kind first becomes supersonic much before the horizon (Fukue 1987; Chakrabarti 1989; Das, Chattopadhyay & Chakrabarti 2001). In this scenario, supersonic matter experiences a centrifugal barrier that causes the piling of matter around the black hole. Eventually, such barrier triggers the discontinuous transition of the flow variables in the form of shock waves provided the relativistic shock conditions are satisfied (Taub 1948). After the shock transition, flow momentarily slows down, however, gradually picks its radial velocity as it moves inward and ultimately enters into the black hole after crossing another critical point usually located close to the horizon. This renders the complete shock induced global accretion solution and solutions of this kind have been examined by several researchers (Fukue 1987; Chakrabarti 1989; Yang & Kafatos 1995; Lu, Gu & Yuan 1999; Becker & Kazanas 2001; Das et al. 2001; Chakrabarti & Das 2004; Fukumura & Tsuruta 2004; Das 2007; Sarkar & Das 2016; Dihingia, Das & Mandal 2018a,b; Dihingia, Das & Nandi 2019). Due to shock compression, post-shock flow becomes hot and dense that results a puffed up torus like structure surrounding the black hole which is equivalently called as post-shock corona (hereafter PSC; Aktar, Das & Nandi 2015). Interestingly, because of the extra thermal energy exists across the shock front, a part of the inflowing matter is deflected at PSC to produce the precursor of the bipolar jets along the rotation axis of the disc (Chakrabarti 1999; Das et al. 2001; Chattopadhyay & Das 2007; Das & Chattopadhyay 2008; Aktar et al. 2015; Aktar et al. 2017; Aktar, Nandi & Das 2019). These findings are also confirmed by the numerical simulations (Molteni, Ryu & Chakrabarti 1996; Lanzafame, Molteni & Chakrabarti 1998; Das et al. 2014; Okuda & Das 2015; Lee et al. 2016).

Incidentally, the same PSC seems to be responsible for the emission of hard radiations observed from the active galactic nuclei (AGNs) and GBH sources. Usually, soft photons from the pre-shock disc are intercepted at the PSC and reprocessed after interacting with the swarm of hot electrons to generate high-energy photons via inverse Comptonization mechanism (Chakrabarti & Titarchuk 1995; Mandal & Chakrabarti 2005, 2008; Iyer, Nandi & Mandal 2015). Moreover, Molteni et al. (1996) showed through numerical simulation that when infall time-scale matches with the cooling time-scale of the accreting matter, resonance oscillation of PSC takes place. As PSC modulates, emergent hard radiations also exhibit non-steady variations which are in general quasi-periodic (QP) in nature (Lee, Ryu & Chattopadhyay 2011; Das et al. 2014; Suková & Janiuk 2015; Suková, Charzyński & Janiuk 2017; Okuda et al. 2019). Hence, the modulation of PSC perhaps be potentially viable to account for the QPO phenomena commonly observed in GBH sources (Belloni, Psaltis & van der Klis 2002; Homan & Belloni 2005; Remillard et al. 2006; Nandi et al. 2012; Iyer et al. 2015; Nandi et al. 2018). In addition, episodic ejections of the matter are also seen as a consequence of PSC undulations (Das et al. 2014). Overall, all the above findings generally supplement the importance of PSC as its role appears to be very much appealing in order to explain the astrophysical sources harbouring black holes.

Being motivated with this, in this work, we study relativistic, viscous, advective, accretion flow around a Kerr black hole. Although 3D time-dependent modelling of general relativistic flow exists in the literature, in this work, we consider steady-state 1.5D flow structure in order to obtain the analytical accretion solutions. Here, we adopt the relativistic hydrodynamic framework to study the flow dynamics (Rezzolla & Zanotti 2013). In addition, we consider the relativistic EoS to describe the accreting plasma (Chandrasekhar 1939; Synge 1957; Cox & Giuli 1968). Incorporating all these, we carry out the critical point analysis and obtain all possible global transonic accretion solutions around the Kerr black holes. Further, we employ the relativistic shock conditions (Taub 1948) and calculate the shock induced global accretion solutions. We study the shock properties, namely shock location ($r_{\rm s}$) and compression ratio (R, measure of density compression across the shock front) in terms of the input parameters, i.e. specific energy ($\mathcal{E}$) and specific angular momentum ($\mathcal{L}$), and examine the role of viscosity (α) and black hole spin (a_k) in deciding the flow characteristics. Moreover, we identify the parameter space in $\mathcal{L}$–$\mathcal{E}$ plane that admits shock and finds that shock parameter space is shrunk with the increase of viscous dissipation. We obtain the critical viscosity parameter ($\alpha^{\rm cri}$) beyond which standing shock solutions disappear and investigate a_k–$\alpha^{\rm cri}$ correlation for shocks. Since $r_{\rm s}$ eventually measures the size of PSC, we phenomenologically calculate the QPO frequency of the PSC modulation ($\nu_{\rm QPO}$) which is equivalent to the inverse of the infall time-scale of post-shock matter. We find that $\nu_{\rm QPO}$ lies in the range of 0.386–1312 Hz for $M_{\rm BH} = 10\,{\rm M}_{\odot}$ and $a_{\rm k} = 0.99$ which seems to be fairly consistent with observation (Remillard et al. 2006; Belloni, Sanna & Méndez 2012; Nandi et al. 2012; Belloni & Stella 2014; Iyer et al. 2015; Motta 2016; Sreehari et al. 2019a,b).

We organize the paper as follows. In Section 2, we present the relativistic hydrodynamics in Kerr space–time and in Section 3, we discuss the modelling of the accretion flow. In Section 4, we carry out the critical point analysis and present the global transonic solutions. In Section 5, we discuss the global solutions with shock, shock properties, shock parameter space, and shock mediated QPOs. Finally, in Section 6, we present the concluding remarks.

2 RELATIVISTIC HYDRODYNAMICS IN KERR SPACE–TIME

We study the hydrodynamics of accretion flow in a generic stationary axisymmetric space–time. Here, there exist two mutually computing killing vectors along (t, ϕ) directions. The remaining space-like coordinates are (r, θ) which are mutually orthogonal and also orthogonal to the two killing vectors at every point in space–time. With this coordinate system, a stationary axisymmetric space–time is written as

$$\begin{aligned} {\rm d}s^2 &= g_{\mu\nu}{\rm d}x^{\mu}{\rm d}x^{\nu} \\ &= g_{tt}{\rm d}t^2 + 2g_{t\phi}{\rm d}t{\rm d}\phi + g_{\phi\phi}{\rm d}\phi^2 + g_{rr}{\rm d}r^2 + g_{\theta\theta}{\rm d}\theta^2, \end{aligned} \tag{1}$$

where the indices μ and ν run from 0 to 3 representing t, r, θ, and ϕ coordinates, respectively. Due to the presence of the two killing

vectors ($l^{\mu}_{t} = \partial_t, l^{\mu}_{\phi} = \partial_{\phi}$), the metric coefficients are in general expressed as the functions of coordinates (r, θ). The non-zero metric elements in Boyer–Lindquist coordinates are given by Boyer & Lindquist (1967),

$$g_{tt} = -\left(1 - \frac{2r}{\Sigma}\right), \quad g_{t\phi} = -\frac{2a_{\rm k} r \sin^2\theta}{\Sigma},$$
$$g_{rr} = \frac{\Sigma}{\Delta}, \quad g_{\theta\theta} = \Sigma, \quad \text{and} \quad g_{\phi\phi} = \frac{A \sin^2\theta}{\Sigma},$$

where $\Sigma = a_{\rm k}^2 \cos^2\theta + r^2$, $\Delta = a_{\rm k}^2 + r^2 - 2r$, and $A = \left(a_{\rm k}^2 + r^2\right)^2 - a_{\rm k}^2 \Delta \sin^2\theta$, respectively. Here, the specific spin of the black hole is written as $a_{\rm k} = J/M_{\rm BH}$, where $M_{\rm BH}$ denotes the mass of the black hole. To express the physical quantities, we use a convenient unit system as $G = M_{\rm BH} = c = 1$, where G is the gravitational constant, c is the speed of light. In this system, length, time, and angular momentum are expressed in unit of $GM_{\rm BH}/c^2$, $GM_{\rm BH}/c^3$, and $GM_{\rm BH}/c$, respectively.

The relativistic hydrodynamics is governed by the conservation energy momentum and particle number as

$$T^{\mu\nu}_{;\nu} = 0, \qquad (\rho u^{\nu})_{;\nu} = 0, \tag{2}$$

where, $T^{\mu\nu}$ denotes the energy momentum tensor, ρ is the density of the flow, and u^{ν} are the components of four velocities supplemented with the constraint $u^{\mu}u_{\mu} = -1$. The energy momentum tensor is written as

$$T^{\mu\nu} = (e + p)u^{\mu}u^{\nu} + pg^{\mu\nu} + \pi^{\mu\nu}, \tag{3}$$

where e and p are the local energy density and local isotropic pressure of the flow. The last term in the right hand side of equation (3) represents the viscous stress tensor. By presuming the shear that gives rise to the viscosity, we have $\pi^{\mu\nu} = -2\eta\sigma^{\mu\nu}$, where η is the viscosity coefficient and the shear tensor is given by Peitz & Appl (1997),

$$\sigma_{\mu\nu} = \frac{1}{2}\left[(u_{\mu;\nu} + u_{\nu;\mu} + a_{\mu}u_{\nu} + a_{\nu}u_{\mu}) - \frac{2}{3}\zeta_{\rm exp}h_{\mu\nu}\right], \tag{4}$$

where a_{μ} $(= u_{\mu;\gamma}u^{\gamma})$ is the four acceleration, $\zeta_{\rm exp}$ $(= u^{\gamma}_{;\gamma})$ is expansion of the fluid world line, and $h_{\mu\nu}$ $(= g_{\mu\nu} + u_{\mu}u_{\nu})$ is the projection tensor. Here, $\eta = \rho\nu$, where ν is the kinetic viscosity.

By projecting the energy momentum conservation equation along the i-th direction, we obtain the Navier–Stokes equation as

$$h^{i}_{\mu}T^{\mu\nu}_{;\nu} = (e + p)u^{\nu}u^{i}_{;\nu} + (g^{i\nu} + u^{i}u^{\nu})p_{,\nu} + h^{i}_{\mu}\pi^{\mu\nu}_{;\nu} = 0, \tag{5}$$

where $i = 1, 2, 3$ and $h^{i}_{\mu}u^{\mu} = 0$. Similarly, the energy generation equation (i.e. first law of thermodynamics) is given by $u_{\mu}T^{\mu\nu}_{;\nu} = 0$ which takes the form,

$$u^{\mu}\left[\left(\frac{e + p}{\rho}\right)\rho_{,\mu} - e_{,\mu}\right] + u_{\mu}\pi^{\mu\nu}_{;\nu} = 0, \tag{6}$$

where the last term in the left hand side of equation (6) represents the viscous heating term and the specific enthalpy of the flow is given by $h = (e + p)/\rho$. To avoid complexity, here we ignore the radiative cooling processes.

In order to solve the hydrodynamical equations that govern the accretion flow around black holes, we require an exact relation among e, ρ, and p, which is commonly known as EoS. For relativistic fluid, we consider an EoS (Chattopadhyay & Ryu 2009) which is given by,

$$e = n_{\rm e}m_{\rm e}f = \frac{\rho}{\tau}f, \tag{7}$$

where

$$f = (2 - \xi)\left[1 + \Theta\left(\frac{9\Theta + 3}{3\Theta + 2}\right)\right] + \xi\left[\frac{1}{\chi} + \Theta\left(\frac{9\Theta + 3/\chi}{3\Theta + 2/\chi}\right)\right]. \tag{8}$$

Here, $n_{\rm e}$ ($n_{\rm p}$), and $m_{\rm e}$ ($m_{\rm p}$) denote the number density and mass of the electron (ion) and $\Theta = k_{\rm B}T/m_{\rm e}c^2$ is the dimensionless temperature of the flow. In addition, $\tau = [2 - \xi(1 - 1/\chi)]$, where we use $\xi = n_{\rm p}/n_{\rm e}$ and $\chi = m_{\rm e}/m_{\rm p}$, respectively. In this work, we use $\xi = 1$ all throughout unless stated otherwise. With this, the polytropic index (N), the ratio of specific heats (Γ) and the sound speed ($a_{\rm s}$) are defined as

$$N = \frac{1}{2}\frac{{\rm d}f}{{\rm d}\Theta}; \quad \Gamma = 1 + \frac{1}{N}; \quad \text{and} \quad a_{\rm s}^2 = \frac{\Gamma p}{e + p} = \frac{2\Gamma\Theta}{f + 2\Theta}. \tag{9}$$

3 MODELLING OF ACCRETION FLOW

We consider a steady, viscous, advective accretion disc confined around the black hole equatorial plane. Hence, for simplicity, we assume $\theta = \pi/2$ and $v_{\theta} \sim 0$ throughout the study. In addition, we define the angular velocity $v_{\phi}^2 = (u^{\phi}u_{\phi})/(-u^{t}u_{t})$ and the associated bulk azimuthal Lorentz factor as $\gamma_{\phi}^2 = 1/(1 - v_{\phi}^2)$. Similarly, we also define the radial three velocity in the corotating frame as $v^2 = \gamma_{\phi}^2 v_r^2$, where $v_r^2 = (u^{r}u_{r})/(-u^{t}u_{t})$ and the associated bulk Lorentz factor $\gamma_v^2 = 1/(1 - v^2)$. Employing these definitions of velocities, we rewrite the second part of the equation (2) in the integrated form as

$$\dot{M} = -4\pi v\gamma_v\rho H\sqrt{\Delta}, \tag{10}$$

where $\dot{M}$ is accretion rate which we treat as global constant and H is the local half-thickness of the disc. Considering the thin-disc approximation, we calculate the functional form of H as (Riffert & Herold 1995; Peitz & Appl 1997)

$$H^2 = \frac{pr^3}{\rho\mathcal{F}}, \qquad \mathcal{F} = \gamma_{\phi}^2\frac{\left(r^2 + a_{\rm k}^2\right)^2 + 2\Delta a_{\rm k}^2}{\left(r^2 + a_{\rm k}^2\right)^2 - 2\Delta a_{\rm k}^2}. \tag{11}$$

In the next, we obtain the radial momentum equation in the corotating frame by setting $i = r$ and is given by

$$v\gamma_v^2\frac{{\rm d}v}{{\rm d}r} + \frac{1}{e + p}\frac{{\rm d}p}{{\rm d}r} + \left(\frac{\partial\Phi}{\partial r}\right)_{\lambda} = 0, \tag{12}$$

where

$$\Phi = \frac{1}{2}\ln\left[\frac{r\Delta}{a_{\rm k}^2(r + 2) - 4a_{\rm k}\lambda + r^3 - \lambda^2(r - 2)}\right],$$

and $\lambda = -u_{\phi}/u_{t}$. In equation (12), following Gammie & Popham (1998) and Popham & Gammie (1998), we neglect the viscous acceleration term in the radial momentum equation.

Employing the killing vectors l^{μ}_{t} and l^{μ}_{ϕ}, we obtain two conserved quantities as

$$\mathcal{E} = -\left(hu_{t} - \frac{2\nu\sigma^{r}_{t}}{u^{r}}\right) \tag{13}$$

and

$$\mathcal{L} = hu_{\phi} - \frac{2\nu\sigma^{r}_{\phi}}{u^{r}}, \tag{14}$$

where, $\nu = \alpha a_{\rm s}H$, α being the viscosity parameter (Gammie & Popham 1998; Popham & Gammie 1998). Since the terms involved in equations (13) and (14) have the dimensions of energy per unit mass and angular momentum, we call $\mathcal{E}$ and $\mathcal{L}$ as global

specific energy and bulk specific angular momentum of the flow, respectively.

Subsequently, we calculate σ^r_ϕ and σ^r_t from equation (4), which are given by

$$2\sigma^r_\phi = u^r_{;\phi} + g^{rr}u_{\phi;r} + a^r u_\phi + a_\phi u^r - \frac{2}{3}\zeta_{\rm exp}u^r u_\phi, \tag{15}$$

and

$$2\sigma^r_t = u^r_{;t} + g^{rr}u_{t;r} + a^r u_t + a_t u^r - \frac{2}{3}\zeta_{\rm exp}u^r u_t. \tag{16}$$

Using the velocity definitions, we rewrite equation (15) and equation (16) in the following forms as

$$2\sigma^r_\phi = \mathcal{A}_1 + \mathcal{A}_2\frac{{\rm d}v}{{\rm d}r} + \mathcal{A}_3\frac{{\rm d}\lambda}{{\rm d}r} \tag{17}$$

and

$$2\sigma^r_t = \mathcal{B}_1 + \mathcal{B}_2\frac{{\rm d}v}{{\rm d}r} + \mathcal{B}_3\frac{{\rm d}\lambda}{{\rm d}r}, \tag{18}$$

where the coefficients $\mathcal{A}_1$, $\mathcal{A}_2$, $\mathcal{A}_3$, $\mathcal{B}_1$, $\mathcal{B}_2$, and $\mathcal{B}_3$ are the functions of the flow variables and their functional forms are given in Appendix A. Since the first-order derivatives of v and λ in the shear tensor yields the governing equations of the relativistic flow as second order, it is difficult to solve them. Therefore, to avoid complexity, we neglect the terms containing the higher order derivatives of v and λ in equation (17) and (18) and with these approximations, we are left with $2\sigma^r_\phi = \mathcal{A}_1$ and $2\sigma^r_t = \mathcal{B}_1$, respectively.

Since $\mathcal{E}$ and $\mathcal{L}$ are conserved quantities, there derivatives vanishes and accordingly, we have

$$\frac{{\rm d}\mathcal{E}}{{\rm d}r} = \mathcal{E}_0 + \mathcal{E}_1\frac{{\rm d}v}{{\rm d}r} + \mathcal{E}_2\frac{{\rm d}\Theta}{{\rm d}r} + \mathcal{E}_3\frac{{\rm d}\lambda}{{\rm d}r} = 0 \tag{19}$$

and

$$\frac{{\rm d}\mathcal{L}}{{\rm d}r} = \mathcal{L}_0 + \mathcal{L}_1\frac{{\rm d}v}{{\rm d}r} + \mathcal{L}_2\frac{{\rm d}\Theta}{{\rm d}r} + \mathcal{L}_3\frac{{\rm d}\lambda}{{\rm d}r} = 0, \tag{20}$$

where $\mathcal{E}_0$, $\mathcal{E}_1$, $\mathcal{E}_2$, $\mathcal{E}_3$, $\mathcal{L}_0$, $\mathcal{L}_1$, $\mathcal{L}_2$, and $\mathcal{L}_3$ are functions of the flow variables and their expression are given in Appendix B.

We simultaneously solve equations (10), (12), (19), and (20) to obtain the wind equation as

$$\frac{{\rm d}v}{{\rm d}r} = \frac{N(r, v, \lambda, \Theta)}{D(r, v, \lambda, \Theta)}, \tag{21}$$

where $N(r, v, \lambda, \Theta)$ and $D(r, v, \lambda, \Theta)$ are the functions of the flow variables and their algebraic expressions are provided in Appendix C. Further, the gradients of Θ and λ is obtained, respectively, as

$$\frac{{\rm d}\Theta}{{\rm d}r} = \frac{(\mathcal{L}_3\mathcal{E}_1 - \mathcal{L}_1\mathcal{E}_3)}{\mathcal{L}_2\mathcal{E}_3 - \mathcal{L}_3\mathcal{E}_2}\frac{{\rm d}v}{{\rm d}r} + \frac{\mathcal{L}_3\mathcal{E}_0 - \mathcal{L}_0\mathcal{E}_3}{\mathcal{L}_2\mathcal{E}_3 - \mathcal{L}_3\mathcal{E}_2}; \tag{22}$$

and

$$\frac{{\rm d}\lambda}{{\rm d}x} = \frac{(\mathcal{L}_2\mathcal{E}_1 - \mathcal{L}_1\mathcal{E}_2)}{\mathcal{L}_3\mathcal{E}_2 - \mathcal{L}_2\mathcal{E}_3}\frac{{\rm d}v}{{\rm d}r} + \frac{\mathcal{L}_2\mathcal{E}_0 - \mathcal{L}_0\mathcal{E}_2}{\mathcal{L}_3\mathcal{E}_2 - \mathcal{L}_2\mathcal{E}_3}, \tag{23}$$

where $\mathcal{E}_i$ and $\mathcal{L}_i$ with $i = 0, 1, 2, 3$ are described in Appendix B.

4 CRITICAL POINT ANALYSIS AND GLOBAL SOLUTIONS

We carry out the critical point analysis following the standard procedure (Dihingia et al. 2018c and references therein) and examine the properties of the critical points in terms of the input parameters of the flow. At the critical point, equation (21) takes ${\rm d}v/{\rm d}r = 0/0$ form, where the conditions $N(r, v, \lambda, \Theta) = 0$ and $D(r, v, \lambda, \Theta) = 0$ are known as the critical point conditions. Applying the l'Hospital rule, we calculate the radial velocity gradient $({\rm d}v/{\rm d}r)_{\rm c}$ at the critical points ($r_{\rm c}$). Depending on the values of $({\rm d}v/{\rm d}r)_{\rm c}$, the nature of the critical points are classified. In reality, $({\rm d}v/{\rm d}r)_{\rm c}$ usually possesses two values. When the values of $({\rm d}v/{\rm d}r)_{\rm c}$ are real and of opposite sign, the critical point is called as saddle type (hereafter 'X-type'). For real and same sign of $({\rm d}v/{\rm d}r)_{\rm c}$ values yield nodal type critical point (hereafter 'N-type'). When both values of $({\rm d}v/{\rm d}r)_{\rm c}$ are imaginary, the nature of the critical point becomes spiral type (hereafter 'O-type'). Based on the above classifications, we examine how the different types of critical points spread along the radial direction. The obtained results are depicted in Fig. 1, where we plot the variation of global specific energy ($\mathcal{E}$) as a function of critical points ($r_{\rm c}$) for three different viscosity parameters as $\alpha = 0.06$, 0.08, and 0.10, respectively. Here, we choose $a_{\rm k} = 0.99$ and $\mathcal{L} = 1.80$. In the figure, viscosity parameters are marked, and solid, dashed, and dotted curves denote the 'X-type', 'N-type', and 'O-type' critical points, respectively. We observe that for a given α, different types of critical points are located along the increasing radial coordinate following the sequence of saddle – nodal – spiral – nodal – saddle types, respectively. For a given $\mathcal{E}$, the flow may have maximum three critical points, out of which one is 'O-type' and the other two may be either 'X-type' or 'N-type' or their combinations depending on the input parameters. Moreover, we find that as the viscosity of the flow is increased, a part of the 'X-type' critical points from both inner and outer regions are gradually replaced by the 'N-type' critical points. In reality, 'X-type' critical points are specially important as the accretion flow around the black holes can only pass through it. In addition, it may be noted that the accretion flows passing through the 'N-type' critical points are found to be unstable (Kato et al. 1993). Moreover, when the critical point resides near the horizon, it is called as inner critical point ($r_{\rm in}$) whereas when it forms far away from the black hole, it is called as outer critical point ($r_{\rm out}$). And, when accretion flow possesses multiple 'X-type' critical points, it may experience discontinuous shock transition in

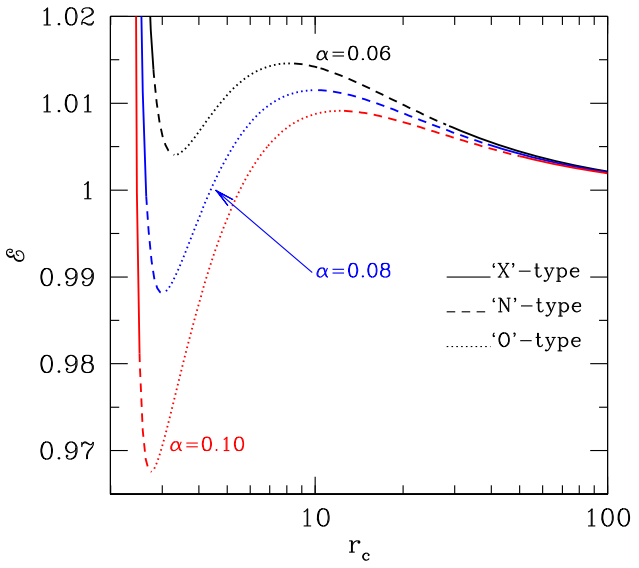

Figure 1. Plots of global specific energy ($\mathcal{E}$) as a function of critical point locations ($r_{\rm c}$) for three different viscosity parameters (α) marked on the figure. Here. we consider $\mathcal{L} = 1.80$ and $a_{\rm k} = 0.99$, respectively. Solid, dotted, and dashed curves represent the results corresponding to saddle (X), nodal (N), and spiral (O) type critical points. See text for details.

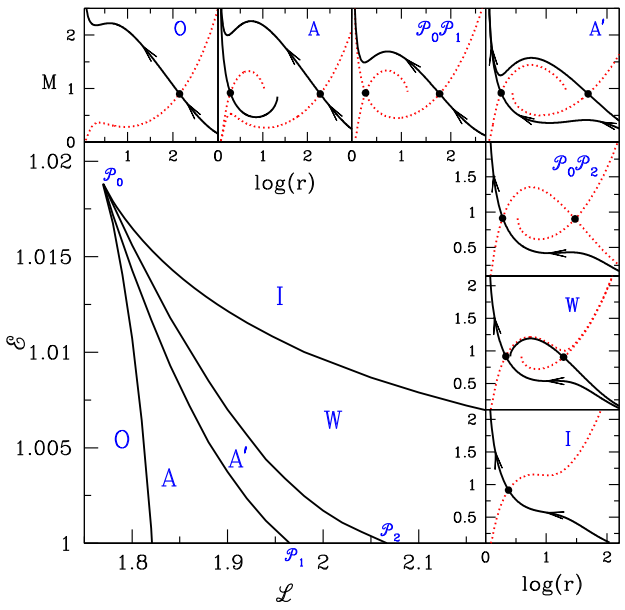

Figure 2. Subdivision of $\mathcal{L}-\mathcal{E}$ parameter space on the basis of the type of accretion solutions. Different regions are marked on the figure as 'O', 'A', '$\mathcal{P}_0\mathcal{P}_1$', 'A′', '$\mathcal{P}_0\mathcal{P}_2$', 'W', and 'I', and the corresponding Mach number ($M = v/a_s$) plots are depicted on the boxes. The filled circle in each boxes represents the critical point locations of the flow and the arrow indicates the overall direction of the flow motion. Here, we choose $a_k = 0.99$ and $\alpha = 0.05$. See text for details.

between the inner and outer critical points, provided the relativistic shock conditions are satisfied (Taub 1948). Accretion solutions of this kind are very much important as they have the potential to explain the observational findings (Chakrabarti & Titarchuk 1995; Wu et al. 2002; Nandi et al. 2012; Iyer et al. 2015; Suková & Janiuk 2015; Fukumura et al. 2016; Suková et al. 2017 and references therein) and therefore, in the subsequent section, we investigate the global shock solutions around the Kerr black holes.

To obtain the accretion solution, one requires to solve the equations (21)–(23) simultaneously. Since the accretion flow around the black hole is necessarily transonic, it is advantageous to start integrating equations (21)–(23) from the critical point itself. Hence, we choose a set of input parameters as $(\mathcal{E}, \mathcal{L}, \alpha, a_k)$ and employing the critical point conditions, we solve equations (13) and (14) to calculate the radial velocity (v_c), temperature (Θ_c), and angular momentum (λ_c) at the critical point (r_c). Using these flow variables, we integrate equations (21)–(23) once inwards from the critical point up to the horizon and then outward up to a large distance equivalent to the outer edge of the disc (r_{edge}). Finally, we join these two parts of the solution to obtain a complete global accretion solution around the black holes. It may be noted that solving equations (21)–(23) using the boundary values supplied at r_{edge} yields the identical accretion solution as described above.

Next, we investigate the general behaviour of the accretion solutions, and for that, we subdivide the $\mathcal{L}-\mathcal{E}$ parameter space according to the nature of the accretion solutions. We find five different types of physically acceptable accretion solutions and therefore, we sub-divide the parameter space in five regions marked as O, A, A′, W, and I in Fig. 2. Here, we choose $a_k = 0.99$ and $\alpha = 0.05$. Typical solutions obtained from these five regions are depicted in the inset boxes which are marked. In each box, Mach number (M) of the flow is plotted as function of the logarithmic radial coordinate (r) where solid curve represents the accretion branch while the dashed curve denotes the wind branch. We find that depending on the input parameters, the flow may contain single or multiple critical points which are shown using the filled circles. In addition, arrows indicate the overall direction of flow motion towards the black hole. *Here, we find a new type of accretion solution* (A′) *where inflowing matter having identical* $(\mathcal{L}, \mathcal{E})$ *has the option to pass through either outer or inner critical points.* In order to resolve the degeneracy of the accretion solution, we calculate the entropy of the flow just outside the horizon and find that solution passing through the inner critical point has high entropy content. Since nature favours the high entropy flow (Becker & Kazanas 2001), solution passing through the inner critical point is physically acceptable. Example of this kind of solution is shown in the box marked A′. Interestingly, supersonic flow after crossing the outer critical point has the possibility to join with the subsonic branch via shock transition (see Section 5), however, we point out that relativistic shock conditions (see equation 24 below) are not satisfied for this type of accretion solutions. We also find accretion solutions with a special topological property where a single integral curve passes through both critical points simultaneously. This type of solutions are found along the line $\mathcal{P}_o - \mathcal{P}_1$ and $\mathcal{P}_o - \mathcal{P}_2$ in the $\mathcal{L}-\mathcal{E}$ parameter space and illustrated in the boxes marked $\mathcal{P}_o\mathcal{P}_1$ and $\mathcal{P}_o\mathcal{P}_2$, respectively. It is noteworthy to mention that accretion solutions depicted in panels marked 'W' and 'I' are identical to the advection dominated accretion flow (ADAF) solutions (Narayan, Kato & Honma 1997 and references therein).

5 ACCRETION SOLUTION WITH SHOCK

In this section, we study the properties of the accretion flow that possesses multiple critical points. In reality, accretion flow begins its journey from the outer edge of the disc (r_{edge}) with negligible radial velocity ($v \ll c$) and gradually gains its radial velocity as it accretes towards the black hole. At the outer critical point (r_{out}), flow experiences smooth sonic state transition from subsonic to the supersonic regime and continues to proceed further. Meanwhile, centrifugal repulsion starts to become profound, and it plays a preponderant role against gravity to slow down the inflowing matter. Because of this, accreting matter piles up in the vicinity of the black hole, and a centrifugal barrier is developed. This process continues unless the centrifugal barrier triggers the discontinuous transitions of the flow variables in the form of a shock wave. Due to the shock transition, the supersonic flow jumps into the subsonic branch and eventually picks up its radial velocity while moving further inwards. Ultimately, accretion flow again becomes supersonic after passing through the inner critical point (r_{in}) before falling into the black hole.

To illustrate the above scenario, we depict a shock induced global accretion solution around a black hole in Fig. 3, where Mach number (M) of the flow is plotted as function of radial coordinate (r). Here, we choose the input parameters as $\mathcal{E} = 1.001$, $\mathcal{L} = 1.90$, $\alpha = 0.05$, and $a_k = 0.99$, respectively and find the inner and outer critical points as $r_{in} = 1.8898$ and $r_{out} = 192.9923$. After crossing r_{out}, the flow has the possibility to enter into the black hole supersonically as shown by the dotted curve. However, flow experiences shock transition in between r_{in} and r_{out} as the relativistic shock conditions are favourable. In reality, the shock solution is preferred over the shock-free solution because of its high entropy content (Becker & Kazanas 2001). We calculate the location of the shock radius using

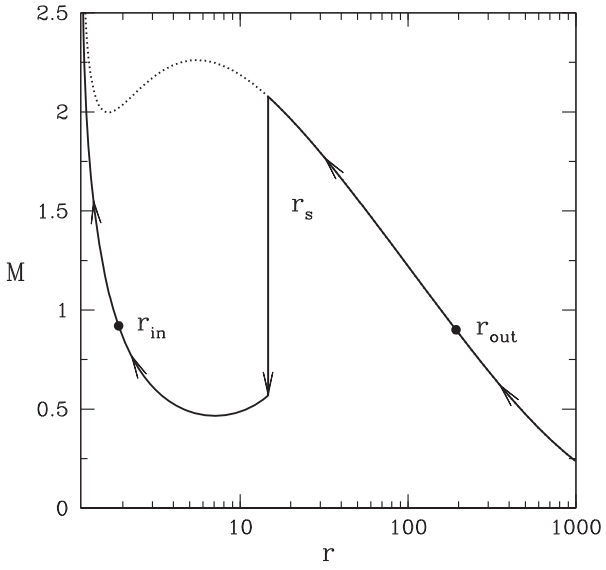

Figure 3. Illustration of a typical shock induced global accretion solution around a Kerr black hole. Here, input parameters are chosen as $\mathcal{L} = 1.90$, $\mathcal{E} = 1.001$, $\alpha = 0.05$, and $a_k = 0.99$, respectively. Inner and outer critical points are calculated as $r_{in} = 1.8898$ and $r_{out} = 192.9923$. Flow encounters shock transition at $r_s = 14.67$ indicated by the vertical arrow. See text for details.

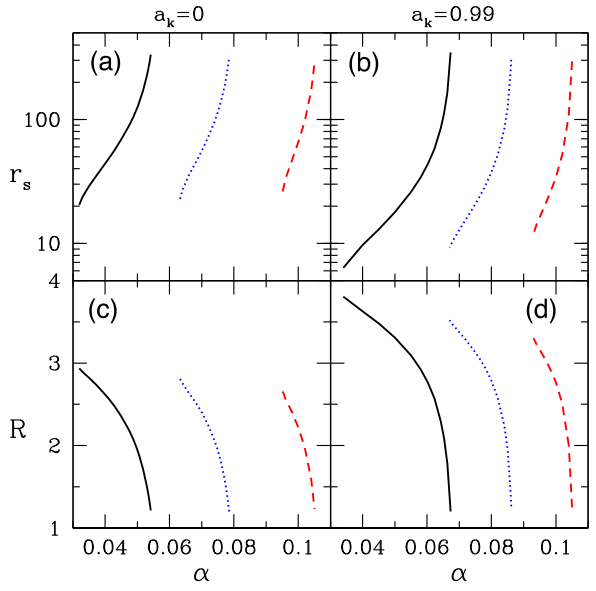

Figure 4. Plots of shock location (r_s) and compression ratio (R) as a function of viscosity parameter (α). Results corresponding to $a_k = 0$ and $a_k = 0.99$ are shown in the left-hand and right-hand panels. For $a_k = 0$, we choose $\mathcal{E} = 1.0002$ and $\mathcal{L} = 2.907$ (solid), 2.737 (dotted), and 2.567 (dashed), respectively. Similarly, for $a_k = 0.99$, we choose $\mathcal{E} = 1.0002$ and $\mathcal{L} = 1.915$ (solid), 1.865 (dotted), and 1.815 (dashed), respectively. See text for details.

the relativistic shock conditions (Taub 1948), which are given by

$$[\rho u^r] = 0, \qquad [(e+p)u^t u^r] = 0, \quad \text{and} \quad [(e+p)u^r u^r + p g^{rr}] = 0, \tag{24}$$

where we assume the shock to be thin and the quantities within the square bracket represent the difference of their values across the shock front. Here, shock location is calculated as $r_s = 14.67$ which is indicated by the vertical arrow and the overall direction of the flow motion is indicated by the arrows.

Next, we examine the various shock properties, and the obtained results are depicted in Fig. 4. In the upper panels, we show the variation of shock location as the function of the viscosity parameter (α) for flows with $\mathcal{E} = 1.0002$. In panel (a), we depict the variation of shock location (r_s) around the non-rotating black hole (Schwarzschild black hole, $a_k = 0$) where solid, dotted, and dashed curves represent the results for $\mathcal{L} = 2.907$ (black), 2.737 (blue), and 2.567 (red), respectively. Similarly, in panel (b), we present the r_s variation for a rotating black hole ($a_k = 0.99$) where solid, dotted, and dashed curves are obtained for $\mathcal{L} = 1.915$ (black), 1.865 (blue), and 1.815 (red), respectively. In panels (a) and (b), we observe that for a given $\mathcal{L}$, shock location recedes away from the black hole as α is increased. This happens because the increase of α enhances the angular momentum transport outwards that boosts the strength of the centrifugal repulsion against the gravity. This eventually compels the shock front to settle down at the larger radii. Interestingly, α cannot be increased indefinitely due to the fact that beyond a critical value of viscosity ($\alpha > \alpha^{cri}$), the shock conditions fail to satisfy for a given set of ($\mathcal{L}$, $\mathcal{E}$, a_k) and therefore standing shock disappears. However, non-steady shock still may continue to present which we shall discuss in the latter part of this section. Due to the shock transition, the post-shock flow (equivalently PSC) becomes hot and compressed where the swarm of hot electrons are readily available. These hot electrons eventually reprocess the soft photons from the pre-shock flow via inverse Comptonization process to produce hard radiations. Thus, it is instructive to examine the amount of density compression across the shock front and study its dependencies on α. For that, we calculate the compression ratio (R), which is defined as the ratio of densities measured immediately after and before the shock transition and is given by $R = \sigma_+/\sigma_-$. The obtained results corresponding to r_s are depicted in panels (c) and (d) for $a_k = 0$ and $a_k = 0.99$, respectively. In both cases, we observe that accreting matter experiences significant compression when shock forms close to the black hole, and the amount of compression gradually decreases with the increase of α. Since shock generally forms at smaller radii around the rotating black holes, the overall compression remains higher for $a_k = 0.99$ in comparison with results for $a_k = 0$ (see panels c and d).

It is useful to study the range of flow parameters that admit the shock induced global accretion solutions around the Kerr black holes. To do that, in Fig. 5, we identify the effective region of the parameter space in the $\mathcal{L} - \mathcal{E}$ plane that provides shock transition. In Fig. 5(a), we present the modification of the parameter space with the increase of the viscosity parameter (α) for an extremely rotating black hole ($a_k = 0.99$). It is clear from the figure that the wide ranges of $\mathcal{E}$ and $\mathcal{L}$ permit shock solutions and the effective region of the parameter space are gradually shrunk as the effect of dissipation, namely, viscosity is increased. In reality, when α is increased, it enhances the effect of viscous dissipation in an accretion flow (see e.g. the second term in the right hand side of equation 13) that causes the decrease of global specific energy ($\mathcal{E}$) of the flow. Similarly, $\mathcal{L}$ is also reduced with the increase of α (see equation 14). As a result, the overall effective area of the parameter space for shock is decreased with α. What is more, is that Fig. 5(a) clearly indicates the existence of the critical viscosity parameter (α^{cri}), beyond this value standing shock solution ceases to exist. It is noteworthy that α^{cri} does not possess a universal value. Instead, it depends on the input parameters, namely $\mathcal{E}$, $\mathcal{L}$, and a_k. In Fig. 5(b), we display the classification of the shock parameter space for various a_k values. Here, we fix $\alpha = 0.1$. We find that the accretion flows around the

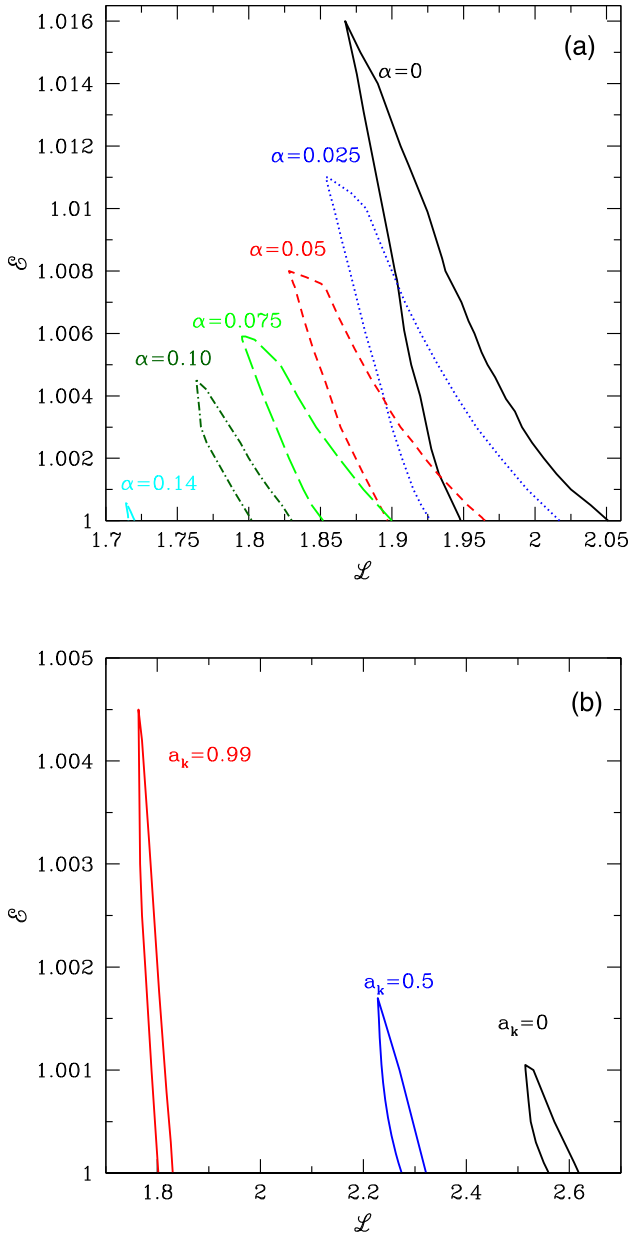

Figure 5. (a) Plots of the shock parameter space in $\mathcal{E}-\mathcal{L}$ plane for different viscosity parameters (α) marked in the figure. Here, we choose $a_{\rm k}=0.99$. The effective domain of the shock parameter space is decreased with α indicating the fact that possibility of shock formation is reduced for dissipative flow. (b) Plots of the $\mathcal{L}-\mathcal{E}$ shock parameter space for three different Kerr parameters marked in the figure. Here, $\alpha=0.1$ is considered. See text for details.

weakly rotating black holes experience shock transitions when $\mathcal{L}$ is relatively high compared to the case of rapidly rotating black holes. In reality, accretion flows with angular momentum lower than the marginally stable value are allowed to enter into the black hole. As $a_{\rm k}$ is increased, the angular momentum at the marginally stable orbit is decreased (Chakrabarti & Mondal 2006) and therefore, low angular momentum flows are in general allowed to accrete on to the rapidly rotating black holes. Note that the spin signature in GBHs and AGNs has already been probed observationally (Reynolds 2019 and references therein).

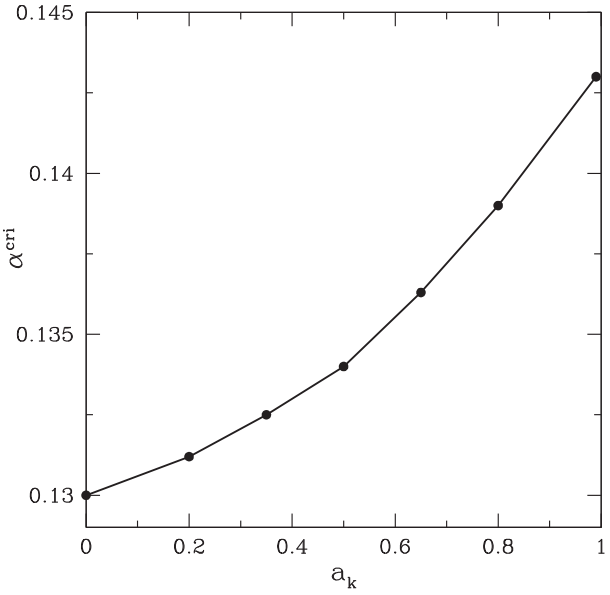

Figure 6. Variation of the critical viscosity parameter ($\alpha^{\rm cri}$) for shock as function of the black hole spin parameter ($a_{\rm k}$). Here, we freely vary the other flow parameters, namely $\mathcal{E}$ and $\mathcal{L}$ to compute $\alpha^{\rm cri}$ for a given a_k. See text for details.

In Fig. 6, we show the variation of the critical viscosity parameter ($\alpha^{\rm cri}$) as function of $a_{\rm k}$. Here, we freely vary both $\mathcal{L}$ and $\mathcal{E}$ and compute $\alpha^{\rm cri}$ for a given a_k. By varying $a_{\rm k}$ in steps, we follow the same procedure to obtain the $\alpha^{\rm cri}$ in the full range of $a_{\rm k}$ values. In the figure, the chosen values of $a_{\rm k}$ are denoted by the filled circles which are further joined with the solid lines. The figure clearly indicates that the overall correlation between $\alpha^{\rm cri}$ and $a_{\rm k}$ remains fairly weak. It may be noted that the obtained $\alpha^{\rm cri}$ are in agreement with the previously reported values from both numerical and observational fronts (Hawley & Krolik 2001, 2002; Penna et al. 2013; Martin et al. 2019 and references therein).

We further explore the usefulness of the shock wave in an accretion flow. It is already discussed that accretion flow contains standing shock wave provided (i) the flow possesses multiple critical points, (ii) the entropy of the flow at the inner critical point ($r_{\rm in}$) is higher than the outer critical point ($r_{\rm out}$), and (iii) the relativistic shock conditions are satisfied (see equation 24). However, the situation may arise for an accretion flow where points (i) and (ii) are fulfilled, but the point (iii) fails to satisfy. In that case, instead of standing shock transition, the shock front demonstrates non-steady behaviour. This particularly happens, possibly due to the resonance oscillation where the post-shock cooling time-scale remains in accord with the infall time-scale of the flow (Molteni et al. 1996). Indeed, the modulation of the shock front does not remain coherent in general, but yields as QP in nature. To quantify the frequency of QPOs of the shock front, we first calculate the infall time-scale of the post-shock flow as $t_{\rm infall}=\int_{r_{\rm s}}^{r_{\rm H}}{\rm d}t=\int_{r_{\rm s}}^{r_{\rm H}}v^{-1}(r){\rm d}r$, where $v(r)$ denotes the post-shock velocity and $r_{\rm H}\,(=1+\sqrt{1-a_k^2})$ is the event horizon. Subsequently, we estimate the frequency of the QP oscillation of the shock front ($\nu_{\rm QPO}$) as $\nu_{\rm QPO}=1/t_{\rm QPO}\sim 1/t_{\rm infall}$ (Molteni et al. 1996; Aktar et al. 2015 and references therein). In general, since QPO frequency is expressed in Hertz, $\nu_{\rm QPO}$ is ultimately multiplied with $c^3/GM_{\rm BH}$. For the purpose of representation, we consider the results depicted in Fig. 4 (upper panel) and calculate the corresponding $\nu_{\rm QPO}$. The obtained results

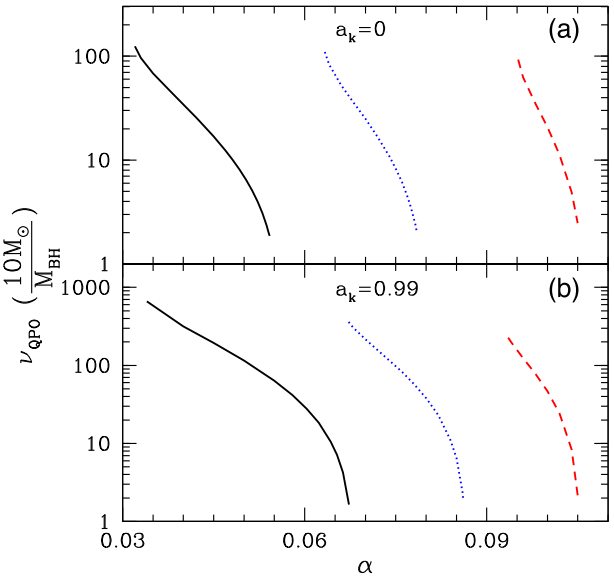

Figure 7. Variation of QPO frequency ($\nu_{\rm QPO}$) as function of viscosity parameter (α) for flows with $\mathcal{E} = 1.0002$. In panel (a), we depict the results for $a_{\rm k} = 0$ where solid, dotted, and dashed curves are for $\mathcal{L} = 2.907$ (black), 2.737 (blus), and 2.567 (red), respectively. In panel (b), we show the results corresponding to $a_{\rm k} = 0.99$ where solid, dotted, and dashed curves are for $\mathcal{L} = 1.915$ (black), 1.865 (blue), and 1.815 (red), respectively. See text for more details.

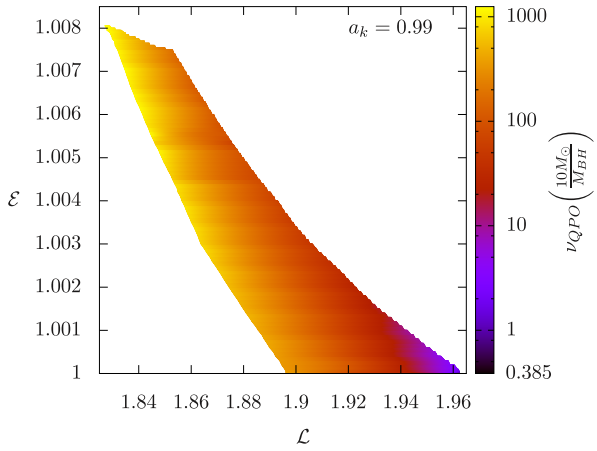

Figure 8. Two-dimensional projection of three-dimensional plot of $[\mathcal{L}, \mathcal{E}, \nu_{\rm QPO}(\frac{10\,{\rm M}_\odot}{M_{\rm BH}})]$ for $a_{\rm k} = 0.99$ and $\alpha = 0.05$. Colour coded bar indicates the frequency range in logarithmic scale. See text for details.

are shown in Fig. 7 where the variation of $\nu_{\rm QPO}$ is plotted as function of α for $\mathcal{E} = 1.0002$. In the upper panel (Fig. 7a), we choose $a_{\rm k} = 0$ and the solid, dotted, and dashed curves represent the results for $\mathcal{L} = 2.907$ (black), 2.737 (blue), and 2.567 (red). Similarly, in the lower panel (Fig. 7b), we show the results for $a_{\rm k} = 0.99$, where solid, dotted, and dashed curves are for $\mathcal{L} = 1.915$ (black), 1.865 (blue), and 1.815 (red), respectively. We observe that $\nu_{\rm QPO}$ decreases with the increase of the α for both non-rotating as well as rapidly rotating black holes. However, the existence of high-frequency QPO (HFQPO) seems to be more viable for the rapidly rotating black holes as shock usually forms closer to the horizon for larger $a_{\rm k}$ values (Aktar et al. 2017; Dihingia et al. 2019, and references therein).

In Fig. 8, we redraw the shock parameter space for $a_{\rm k} = 0.99$ and $\alpha = 0.05$, where the two-dimensional projection of the three-dimensional plot spanned with $\mathcal{L}$, $\mathcal{E}$, and $\nu_{\rm QPO}$ is depicted. In the right side of the figure, the colour coded vertical bar indicates the range of $\nu_{\rm QPO}$ (in units of $10\,{\rm M}_\odot/M_{\rm BH}$) obtained by using the post-shock velocity profile as described above. We find that for a given $\mathcal{E}$, accretion flow generally exhibits HFQPOs provided $\mathcal{L}$ is relatively small and vice versa. These findings are in agreement with the results of Fig. 7, as shocks generally settle down at smaller radii for flows with lower $\mathcal{L}$ (see Fig. 4) that yield high $\nu_{\rm QPO}$ values. Also, we observe that Fig. 8 encompasses the QPO frequencies starting from milli-Hz (∼0.386 Hz) to kilo-Hz (∼1312 Hz) range for a $10\,{\rm M}_\odot$ black hole. This evidently indicates that the present formalism would be capable of rendering the QPO frequencies observed from the GBH sources (Remillard et al. 1999; Strohmayer 2001; Belloni et al. 2002, 2005; Remillard et al. 2006; Altamirano & Belloni 2012; Belloni et al. 2012; Nandi et al. 2012; Belloni & Altamirano 2013; Iyer et al. 2015; Sreehari et al. 2019b, and references therein).

At the end, we compare theoretically obtained maximum QPO frequency ($\nu^{\rm max}_{\rm QPO}$) with observed HFQPOs. For that, we choose two well-studied GBH sources, namely GRS 1915+105 and GRO J1655−40 as they are known to exhibit HFQPOs. For GRS 1915+105, the mass and spin are well constrained and this source exhibits HFQPO as $\nu^{\rm obs}_{\rm QPO} \sim 67.3 \pm 2$ Hz (Morgan, Remillard & Greiner 1997; Belloni & Altamirano 2013). In this work, we consider $M_{\rm BH} = 10.1 \pm 0.6$ M$_\odot$ (Steeghs et al. 2013) and $a_{\rm k} = 0.99$ (Miller et al. 2013). Using these fundamental parameters, we calculate the maximum QPO frequency ($\nu^{\rm max}_{\rm QPO}$) as function of viscosity parameter (α). This result is shown in the upper panel of Fig. 9, where the shaded region (in purple) is obtained considering the uncertainty in the estimate of the source mass. The figure indicates that $\nu^{\rm obs}_{\rm QPO} < \nu^{\rm max}_{\rm QPO}$ for $\alpha \lesssim 0.135$. For GRO J1655−40, the source mass is estimated using the dynamical method as $M_{\rm BH} = 5.1$–6.3 M$_\odot$ (Greene, Bailyn & Orosz 2001; Beer & Podsiadlowski 2002). Interestingly, contradictory claims appear in the measurement of the spin parameter (Abramowicz & Kluźniak 2001; Shafee et al. 2006; Motta et al. 2014; Aktar et al. 2017; Dihingia et al. 2019) which is yet to be settled. Hence, in this work, we consider $0.8 \leq a_{\rm k} \leq 0.99$ for representation and calculate $\nu^{\rm max}_{\rm QPO}$ as before. The obtained results are depicted in the lower panel of Fig. 9, where $a_{\rm k}$ values are marked and shaded regions (in purple and orange) are because of the mass range of GRO J1655−40. We observe that for this source, when $a_{\rm k} = 0.99$ (rapidly rotating), $\nu^{\rm obs}_{\rm QPO} < \nu^{\rm max}_{\rm QPO}$ with $\alpha \lesssim 0.125$, whereas for $a_{\rm k} = 0.8$ (moderately rotating), $\nu^{\rm obs}_{\rm QPO} < \nu^{\rm max}_{\rm QPO}$ with $\alpha \lesssim 0.1$.

It may be noted that the estimated ranges of α for the above sources (GRS 1915+105 and GRO J1655−40) fairly are in agreement with the results of numerical simulations (Hawley & Krolik 2001, 2002; Penna et al. 2013).

6 CONCLUSIONS

In this work, we study the relativistic viscous accretion flow around a Kerr black hole considering the general relativistic approach. We compose the governing equations that describe the motion of the accreting matter in an accretion disc and employing the boundary parameters, we solve these equations to obtain the transonic accretion solutions. We find that depending on the flow parameters, accretion flows may contain multiple critical points and such flows are astrophysically important as they may harbour shock waves

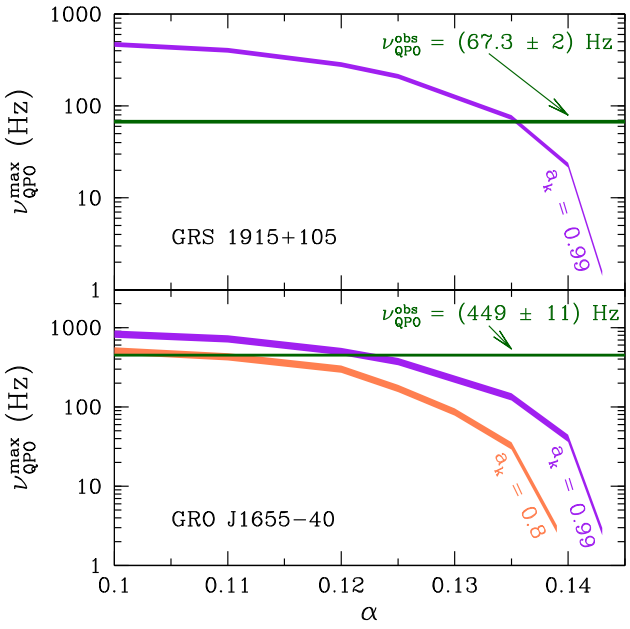

Figure 9. Comparison of theoretically calculated maximum QPO frequency (ν_{QPO}^{max}) with observed HFQPOs. In the upper panel, we present the results for GRS 1915+105, where shaded region (in purple) are obtained for $a_k = 0.99$ and $M_{BH} = 10.1 \pm 0.6$ $M_\odot$. The horizontal thick line (green) indicates the observed HFQPO as $\nu_{QPO}^{obs} \sim 67.3 \pm 2$ Hz. In the lower panel, results corresponding to GRO J1655−40 is shown. Here, shaded regions are for $a_k = 0.99$ (purple) and $a_k = 0.8$ (orange), respectively, with $M_{BH} = 5.1$–6.3 $M_\odot$. The horizontal thick line (green) indicates the observed HFQPO as $\nu_{QPO}^{obs} \sim 449 \pm 11$ Hz. See text for details.

provided the relativistic shock conditions are favourable. Below, we summarize our findings based on this work.

(1) We study the transonic properties of the accretion flow and find that flows continue to possess more than one critical point when the input parameters are chosen appropriately. We obtain all the possible accretion solutions around the Kerr black holes by tuning the flow parameters and separate the parameter space in the $\mathcal{L} - \mathcal{E}$ plane according to the nature of the accretion solutions (see Fig. 2). It may be noted that we find a new type of accretion solution (A' in Fig. 2).

(2) To the best of our knowledge, for the first time, we show that relativistic viscous accretion solutions around the Kerr black holes experience discontinuous transitions in the flow variables in the form of shock waves provided the relativistic shock conditions are satisfied (see Fig. 3). We study the properties of shock waves, namely shock location (r_s) and compression ratio (R) and examine their dependencies on the input parameters. We observe that shock fronts in general settle down to the smaller radii when the flows accrete on to the rapidly rotating black holes and vice versa. As r_s is small, flow experiences more compression at the shock discontinuity resulting in high values of R (see Fig. 4).

(3) We make an effort to constrain the range of the input parameters that admit shock induced global accretion solutions around the Kerr black holes. We find that standing shocks are permitted for the wide ranges of the $\mathcal{L}$ and $\mathcal{E}$ for inviscid flow. As the viscosity is increased, the ranges of parameters are gradually shrunk in the lower $\mathcal{L}$ and $\mathcal{E}$ domain, and ultimately standing shock disappears when the viscosity exceeds its critical limit (α^{cri}) (see Fig. 5). We calculate α^{cri} by freely varying the input parameters and observe that α^{cri} varies with a_k weakly (see Fig. 6).

(4) It is intriguing to note that accretion flow often initiates the modulation of its inner part, particularly when the relativistic shock conditions are not favourable, but the entropy of the inner critical point (r_{in}) is higher than the outer critical point (r_{out}). The outcome of this effect results the QPO of emitted radiations that are commonly observed from the GBH sources during their different evolutionary phases. Using a phenomenological approach, we estimate the frequency of the QPO (ν_{QPO}) and study the role of the input parameters on ν_{QPO}. With this, we identify the shock parameter space in $\mathcal{L} - \mathcal{E}$ plane in terms of the ν_{QPO} and observe that the present formalism is capable of explaining the QPOs in the frequency range starting from milli-Hz to kilo-Hz (see Fig. 8). Using our model formalism, we phenomenologically estimate the ranges of viscosity parameter as $\alpha \lesssim 0.135$ and 0.125 for GRS 1915+105 and GRO J1655−40, respectively, that could possibly account for the observed HFQPOs (Fig. 9). It may be noted that the above findings are purely indicative. For the quantitative estimates of the range of viscosity parameters, time-dependent numerical modelling is required which is beyond the scope of this paper.

Finally, we point out that in this paper, we have imposed several assumptions and approximations. For example, we neglect the radiative cooling processes, namely bremsstrahlung, synchrotron, and Compton coolings mechanisms although their presence are inevitable in the accretion disc. Furthermore, we assume that strong coupling exists between ion and electron that renders the flow to maintain a single temperature all throughout the disc. However, because of the weak ion–electron coupling, the two-temperature flow structure seems to be viable at least in the inner part of the disc. Moreover, we ignore the mass-loss from the disc as well. Although the implementation of all these aspects is beyond the scope of this work, however, we plan to incorporate them in our future works.

ACKNOWLEDGEMENTS

Authors thank the anonymous reviewer for constructive comments and suggestions that help to improve the quality of the paper. AN thanks GD, SAG; DD, PDMSA and Director, URSC for encouragement and continuous support to carry out this research. ID thanks Bibhas Ranjan Mahji, Rashidul Islam, Purusottam Ghosh and Pankaj Saha for fruitful discussions.

REFERENCES

Abramowicz M. A., Kluźniak W., 2001, A&A, 374, L19
Aktar R., Das S., Nandi A., 2015, MNRAS, 453, 3414
Aktar R., Das S., Nandi A., Sreehari H., 2017, MNRAS, 471, 4806
Aktar R., Nandi A., Das S., 2019, Ap&SS, 364, 22
Altamirano D., Belloni T., 2012, ApJ, 747, L4
Becker P. A., Kazanas D., 2001, ApJ, 546, 429
Beer M. E., Podsiadlowski P., 2002, MNRAS, 331, 351
Belloni T., Psaltis D., van der Klis M., 2002, ApJ, 572, 392
Belloni T., Homan J., Casella P., van der Klis M., Nespoli E., Lewin W. H. G., Miller J. M., Méndez M., 2005, A&A, 440, 207
Belloni T. M., Altamirano D., 2013, MNRAS, 432, 10
Belloni T. M., Stella L., 2014, Space Sci. Rev., 183, 43
Belloni T. M., Sanna A., Méndez M., 2012, MNRAS, 426, 1701
Boyer R. H., Lindquist R. W., 1967, J. Math. Phys., 8, 265
Chakrabarti S., Titarchuk L. G., 1995, ApJ, 455, 623
Chakrabarti S. K., 1989, ApJ, 347, 365
Chakrabarti S. K., 1996a, MNRAS, 283, 325
Chakrabarti S. K., 1996b, ApJ, 471, 237

Chakrabarti S. K., 1999, A&A, 351, 185
Chakrabarti S. K., Das S., 2004, MNRAS, 349, 649
Chakrabarti S. K., Mondal S., 2006, MNRAS, 369, 976
Chandrasekhar S., 1939, An Introduction to the Study of Stellar Structure. Univ. Chicago Press, Chicago, IL
Chattopadhyay I., Chakrabarti S. K., 2011, Int. J. Mod. Phys. D, 20, 1597
Chattopadhyay I., Das S., 2007, New A, 12, 454
Chattopadhyay I., Kumar R., 2016, MNRAS, 459, 3792
Chattopadhyay I., Ryu D., 2009, ApJ, 694, 492
Cox J. P., Giuli R. T., 1968, Principles of Stellar Structure. Gordon and Breach, New York
Das S., 2007, MNRAS, 376, 1659
Das S., Chattopadhyay I., 2008, New Astron., 13, 549
Das S., Chattopadhyay I., Nandi A., Chakrabarti S. K., 2001, A&A, 379, 683
Das S., Chattopadhyay I., Chakrabarti S. K., 2001, ApJ, 557, 983
Das S., Chattopadhyay I., Nandi A., Molteni D., 2014, MNRAS, 442, 251
Dihingia I. K., Das S., Mandal S., 2018a, J. Astrophys. Astron., 39, 6
Dihingia I. K., Das S., Mandal S., 2018b, MNRAS, 475, 2164
Dihingia I. K., Das S., Maity D., Chakrabarti S., 2018c, Phys. Rev. D, 98, 083004
Dihingia I. K., Das S., Nandi A., 2019, MNRAS, 484, 3209
Frank J., King A., Raine D. J., 2002, Accretion Power in Astrophysics: Third Edition. Cambridge Univ. Press, Cambridge, p. 398
Fukue J., 1987, PASJ, 39, 309
Fukue J., 2019, MNRAS, 483, 2538
Fukumura K., Tsuruta S., 2004, ApJ, 611, 964
Fukumura K., Hendry D., Clark P., Tombesi F., Takahashi M., 2016, ApJ, 827, 31
Gammie C. F., Popham R., 1998, ApJ, 498, 313
Greene J., Bailyn C. D., Orosz J. A., 2001, ApJ, 554, 1290
Hawley J. F., Krolik J. H., 2001, ApJ, 548, 348
Hawley J. F., Krolik J. H., 2002, ApJ, 566, 164
Homan J., Belloni T., 2005, Ap&SS, 300, 107
Iyer N., Nandi A., Mandal S., 2015, ApJ, 807, 108
Kato S., Wu X.-B., Yang L.-T., Yang Z.-L., 1993, MNRAS, 260, 317
Kumar R., Chattopadhyay I., 2017, MNRAS, 469, 4221
Lanzafame G., Molteni D., Chakrabarti S. K., 1998, MNRAS, 299, 799
Lee S.-J., Ryu D., Chattopadhyay I., 2011, ApJ, 728, 142
Lee S.-J., Chattopadhyay I., Kumar R., Hyung S., Ryu D., 2016, ApJ, 831, 33
Lu J.-F., Gu W.-M., Yuan F., 1999, ApJ, 523, 340
Mandal S., Chakrabarti S. K., 2005, A&A, 434, 839
Mandal S., Chakrabarti S. K., 2008, ApJ, 689, L17
Martin R. G., Nixon C. J., Pringle J. E., Livio M., 2019, New Astron., 70, 7
Miller J. M. et al., 2013, ApJ, 775, L45
Molteni D., Ryu D., Chakrabarti S. K., 1996, ApJ, 470, 460
Morgan E. H., Remillard R. A., Greiner J., 1997, ApJ, 482, 993
Motta S. E., 2016, Astron. Nachr., 337, 398
Motta S. E., Belloni T. M., Stella L., Muñoz-Darias T., Fender R., 2014, MNRAS, 437, 2554
Nandi A. et al., 2018, Ap&SS, 363, 90
Nandi A., Debnath D., Mandal S., Chakrabarti S. K., 2012, A&A, 542, A56
Narayan R., Kato S., Honma F., 1997, ApJ, 476, 49
Novikov I. D., Thorne K. S., 1973, in Dewitt C., Dewitt B. S., eds, Black Holes (Les Astres Occlus), Gordon and Breach, New York. p. 343
Okuda T., Das S., 2015, MNRAS, 453, 147
Okuda T., Singh C. B., Das S., Aktar R., Nandi A., de Gouveia Dal Pino E. M., 2019, PASJ, 71, 49
Peitz J., Appl S., 1997, MNRAS, 286, 681
Penna R. F., Sądowski A., Kulkarni A. K., Narayan R., 2013, MNRAS, 428, 2255
Popham R., Gammie C. F., 1998, ApJ, 504, 419
Remillard R. A., Morgan E. H., McClintock J. E., Bailyn C. D., Orosz J. A., 1999, ApJ, 522, 397
Remillard R. A., McClintock J. E., Orosz J. A., Levine A. M., 2006, ApJ, 637, 1002
Reynolds C. S., 2019, NatAs, 3, 41
Rezzolla L., Zanotti O., 2013, Relativistic Hydrodynamics, Oxford University Press, UK
Riffert H., Herold H., 1995, ApJ, 450, 508
Sarkar B., Das S., 2016, MNRAS, 461, 190
Shafee R., McClintock J. E., Narayan R., Davis S. W., Li L.-X., Remillard R. A., 2006, ApJ, 636, L113
Sreehari H., Iyer N., Radhika D., Nandi A., Mandal S., 2019a, Adv. Space Res., 63, 1374
Sreehari H., Ravishankar B. T., Iyer N., Agrawal V. K., Katoch T. B., Mandal S., Nandi A., 2019b, MNRAS, 487, 928
Steeghs D., McClintock J. E., Parsons S. G., Reid M. J., Littlefair S., Dhillon V. S., 2013, ApJ, 768, 185
Strohmayer T. E., 2001, ApJ, 552, L49
Suková P., Janiuk A., 2015, MNRAS, 447, 1565
Suková P., Charzyński S., Janiuk A., 2017, MNRAS, 472, 4327
Synge J. L., 1957, The Relativistic Gas, Vol. 32. North-Holland Publishing Co., Amsterdam
Taub A. H., 1948, Phys. Rev., 74, 328
Wu K. et al., 2002, ApJ, 565, 1161
Yang R., Kafatos M., 1995, A&A, 295, 238

APPENDIX A: EXPLICIT EXPRESSION OF VISCOUS STRESS

The components of viscous stresses σ_ϕ^r and σ_t^r in corotating frame are expressed as

$$2\sigma_\phi^r = \mathcal{A}_1 + \mathcal{A}_2\frac{\mathrm{d}v}{\mathrm{d}r} + \mathcal{A}_3\frac{\mathrm{d}\lambda}{\mathrm{d}r}, \tag{A1}$$

$$2\sigma_t^r = \mathcal{B}_1 + \mathcal{B}_2\frac{\mathrm{d}v}{\mathrm{d}r} + \mathcal{B}_3\frac{\mathrm{d}\lambda}{\mathrm{d}r}, \tag{A2}$$

where

$$\mathcal{A}_1 = \frac{(\mathcal{A}_{11}+\mathcal{A}_{12}+\mathcal{A}_{13})\,\gamma_v^3}{\mathcal{S}},$$

$$\mathcal{A}_2 = \frac{4\Delta\lambda v\gamma_v^5}{3r^2\sqrt{\mathcal{P}\mathcal{Q}}},$$

$$\mathcal{A}_3 = \frac{\Delta\gamma_v^3}{r^2\mathcal{P}^{3/2}\sqrt{\mathcal{Q}}},$$

$$\mathcal{B}_1 = \frac{(\mathcal{B}_{11}+\mathcal{B}_{12})\,\gamma_v^3}{\mathcal{S}},$$

$$\mathcal{B}_2 = -\frac{4\Delta v\gamma_v^5}{3r^2\sqrt{P\mathcal{Q}}}, \text{ and}$$

$$\mathcal{B}_3 = -\frac{(2a_\mathrm{k}+(r-2)\lambda)\gamma_v^3}{r^3\,(\mathcal{P}\mathcal{Q})^{3/2}}.$$

Here, we write

$$\mathcal{A}_{11} = -3a_\mathrm{k}r\left(a_\mathrm{k}^2+3r^2\right)\left(a_\mathrm{k}^2(r+2)+r^3\right),$$

$$\mathcal{A}_{12} = rv^2\left(3a_\mathrm{k}\left(a_\mathrm{k}^2+3r^2\right)-2\left(a_\mathrm{k}^2(r+3)-(r-3)r^2\right)\lambda\right) \times\left(a_\mathrm{k}^2(r+2)-\lambda(4a_\mathrm{k}+(r-2)\lambda)+r^3\right),$$

$$\mathcal{A}_{13} = -6a_\mathrm{k}\lambda^2\left(a_\mathrm{k}^2(r+1)(r+4)-a_\mathrm{k}(r+2)\lambda+4r^3\right) +6\lambda\left(a_\mathrm{k}^2(r+2)+r^3\right)\left(a_\mathrm{k}^2(2r+1)-(r-3)r^3\right),$$

$$\mathcal{B}_{11} = 2rv^2\left((r-3)\left(a_\mathrm{k}^2+2r^2\right)+3a_\mathrm{k}\lambda\right) \times\left(a_\mathrm{k}^2(r+2)-\lambda(4a_\mathrm{k}+(r-2)\lambda)+r^3\right)$$

$$\mathcal{B}_{12} = 3(2a_{\rm k} + (r-2)\lambda) \times \left(a_{\rm k}^3(r-2)+2\lambda\left(a_{\rm k}^2(1-2r)+a_{\rm k}r\lambda+(r-3)r^3\right)+5a_{\rm k}r^3\right)$$

$$\mathcal{P} = \frac{a_{\rm k}^2(r+2)-\lambda(4a_{\rm k}+(r-2)\lambda)+r^3}{a_{\rm k}^2(r+2)-2a_{\rm k}\lambda+r^3},$$

$$\mathcal{Q} = \frac{a_{\rm k}^2(r+2)-2a_{\rm k}\lambda+r^3}{r\Delta}, \text{ and}$$

$$\mathcal{S} = 3r^6\Delta\left(\mathcal{P}\mathcal{Q}\right)^{3/2},$$

where quantities have their usual meanings.

APPENDIX B: DETAIL EXPRESSIONS OF THE GOVERNING EQUATIONS

The radial momentum, angular momentum, and energy equations are obtained as

$$\mathcal{R}_0 + \mathcal{R}_1\frac{{\rm d}v}{{\rm d}r} + \mathcal{R}_2\frac{{\rm d}\Theta}{{\rm d}r} + \mathcal{R}_3\frac{{\rm d}\lambda}{{\rm d}r} = 0, \tag{B1}$$

$$\mathcal{E}_0 + \mathcal{E}_1\frac{{\rm d}v}{{\rm d}r} + \mathcal{E}_2\frac{{\rm d}\Theta}{{\rm d}r} + \mathcal{E}_3\frac{{\rm d}\lambda}{{\rm d}r} = 0, \text{ and} \tag{B2}$$

$$\mathcal{L}_0 + \mathcal{L}_1\frac{{\rm d}v}{{\rm d}r} + \mathcal{L}_2\frac{{\rm d}\Theta}{{\rm d}r} + \mathcal{L}_3\frac{{\rm d}\lambda}{{\rm d}r} = 0, \tag{B3}$$

where

$$\mathcal{R}_0 = \left(\frac{\partial\Phi}{\partial r}\right)_\lambda + \frac{\Theta}{f+2\Theta}\left[\frac{2-2r}{a_{\rm k}^2+(r-2)r} + \frac{\mathcal{F}_1'}{\mathcal{F}_1} - \frac{3}{r} - \frac{2\lambda\left(a_{\rm k}^3+\lambda\left(-2a_{\rm k}^2+a_{\rm k}\lambda+(r-3)r^2\right)+3a_{\rm k}r^2\right)}{\mathcal{R}_{\rm D}}\right],$$

$$\mathcal{R}_1 = v\gamma_v^2 - \frac{2\Theta\gamma_v^2}{v(f+2\Theta)},$$

$$\mathcal{R}_2 = \frac{1}{f+2\Theta},$$

$$\mathcal{R}_3 = \frac{2\Theta\left\{(r-2)\lambda\left(a_{\rm k}^2(r+2)-a_{\rm k}\lambda+r^3\right)+a_{\rm k}\left(a_{\rm k}^2(r+2)+r^3\right)\right\}}{(f+2\Theta)\mathcal{R}_{\rm D}},$$

$$\mathcal{L}_0 = \frac{\gamma_v h\lambda\mathcal{L}_{\rm N}\sqrt{\mathcal{Q}}}{\left(a_{\rm k}^2(r+2)-2a_{\rm k}\lambda+r^3\right)^2\mathcal{P}^{3/2}} + \frac{\partial\left(\Lambda\mathcal{A}_1\right)}{\partial r},$$

$$\mathcal{L}_1 = \frac{h\lambda v\gamma_v^3}{\sqrt{\mathcal{P}\mathcal{Q}}} + \frac{\partial\left(\Lambda\mathcal{A}_1\right)}{\partial v},$$

$$\mathcal{L}_2 = \frac{2\gamma_v\lambda(N+1)}{\tau\sqrt{\mathcal{P}\mathcal{Q}}} + \frac{\partial\left(\Lambda\mathcal{A}_1\right)}{\partial\Theta},$$

$$\mathcal{L}_3 = \frac{h\gamma_v}{\mathcal{P}^{3/2}\sqrt{\mathcal{Q}}} + \frac{\partial\left(\Lambda\mathcal{A}_1\right)}{\partial\lambda},$$

$$\mathcal{E}_0 = \frac{h\gamma_v\sqrt{\mathcal{Q}}}{\left(a_{\rm k}^2(r+2)-2a_{\rm k}\lambda+r^3\right)^2\mathcal{P}^{3/2}} + \frac{\partial\left(\Lambda\mathcal{B}_1\right)}{\partial r},$$

$$\mathcal{E}_1 = \frac{hv\gamma_v^3}{\sqrt{\mathcal{P}\mathcal{Q}}} + \frac{\partial\left(\Lambda\mathcal{B}_1\right)}{\partial v},$$

$$\mathcal{E}_2 = \frac{2(N+1)\gamma_v}{\tau\sqrt{P\,Q}} + \frac{\partial\left(\Lambda\mathcal{B}_1\right)}{\partial\Theta}, \text{ and}$$

$$\mathcal{E}_3 = \frac{h(2a_{\rm k}+(r-2)\lambda)\gamma_v}{r\Delta\mathcal{P}^{3/2}\mathcal{Q}^{3/2}} + \frac{\partial\left(\Lambda\mathcal{B}_1\right)}{\partial\lambda}.$$

Here, we write

$$\mathcal{R}_{\rm D} = \left(a_{\rm k}^2(r+2)-2a_{\rm k}\lambda+r^3\right) \times \left(a_{\rm k}^2(r+2)-\lambda(4a_{\rm k}+(r-2)\lambda)+r^3\right)$$

$$\mathcal{L}_{\rm N} = a_{\rm k}^4 - 2a_{\rm k}\left(a_{\rm k}^2+r(3r-4)\right)\lambda + \left(a_{\rm k}^2-(r-2)^2r\right)\lambda^2 + 2a_{\rm k}^2(r-2)r + r^4,$$

$$\Phi = \frac{1}{2}\ln\left[\frac{r\Delta}{a_{\rm k}^2(r+2)-4a_{\rm k}\lambda+r^3-\lambda^2(r-2)}\right],$$

$$\mathcal{F}_1 = \frac{\left(a_{\rm k}^2+r^2\right)^2+2a_{\rm k}^2\Delta}{\left(a_{\rm k}^2+r^2\right)^2-2a_{\rm k}^2\Delta}, \text{ and}$$

$$\Lambda = \frac{\alpha a_{\rm s}Hr}{v\gamma_v\sqrt{\Delta}},$$

where quantities have their usual meanings.

APPENDIX C: EXPLICIT EXPRESSION OF WIND EQUATION

We obtain the wind equation which is given by

$$\frac{{\rm d}v}{{\rm d}r} = \frac{\mathcal{N}(r,v,\lambda,\Theta)}{\mathcal{D}(r,v,\lambda,\Theta)}, \tag{C1}$$

where

$$\mathcal{N}(r,v,\lambda,\Theta) = \mathcal{L}_3\left(\mathcal{E}_2\mathcal{R}_0-\mathcal{E}_0\mathcal{R}_2\right)+\mathcal{L}_2\left(\mathcal{E}_0\mathcal{R}_3-\mathcal{E}_3\mathcal{R}_0\right) + \mathcal{L}_0\left(\mathcal{E}_3\mathcal{R}_2-\mathcal{E}_2\mathcal{R}_3\right) \text{ and}$$

$$\mathcal{D}(r,v,\lambda,\Theta) = \mathcal{L}_3\left(\mathcal{E}_1\mathcal{R}_2-\mathcal{E}_2\mathcal{R}_1\right)+\mathcal{L}_1\left(\mathcal{E}_2\mathcal{R}_3-\mathcal{E}_3\mathcal{R}_2\right) + \mathcal{L}_2\left(\mathcal{E}_3\mathcal{R}_1-\mathcal{E}_1\mathcal{R}_3\right).$$

This paper has been typeset from a TEX/LATEX file prepared by the author.